


 Cite this: *RSC Adv.*, 2026, 16, 16874

# Atmosphere-dependent synthesis and crystallization behavior of silica nanoparticles derived from rice husk biomass

 Fuad Hama Shareef Radha,<sup>a</sup> Mohammad Tahir Kareem<sup>a</sup> and Omed Gh. Abdullah \*<sup>b</sup>

This work on sustainable nanomaterials focuses on their green synthesis methods using cheap and renewable precursors. In this study, silica nanoparticles (SiO<sub>2</sub> NPs) were prepared from agro-waste biomass rice husk through an environmentally safe extraction process. Three controlled ashing conditions were used to determine the effect of the processing atmosphere on the end-product SiO<sub>2</sub> NPs. Besides offering a reliable route to silica recovery, this process allowed one to control the phase and structure of the final nanostructures. The formation of high-purity SiO<sub>2</sub> NPs was confirmed through characterization with the assistance of X-ray diffraction (XRD), Fourier transform infrared (FTIR) spectroscopy, field-emission-scanning electron microscopy (FE-SEM), energy-dispersive X-ray (EDX) spectroscopy, transmission electron microscopy (TEM) and zeta potential measurements. The as-synthesized nanoparticles exhibited a predominantly amorphous nature, with particle diameters ranging from 20 to 37 nm, and consisted of aggregated spherical grains. Post-synthesis thermal treatment at 1000 °C effectively induced a clear amorphous-to-crystalline phase change in the silica structure. This reaction caused the emergence of cristobalite-type silica, confirming that the structural stage and consequent morphology can be accurately engineered by the thermal treatment of the green-synthesised NPs. This study extensively highlights the enormous potential of rice husk biomass as a dual-use feedstock for waste valorization and the scalable production of SiO<sub>2</sub> NPs, which can be further utilized for phase-associated functional applications.

Received 14th January 2026

Accepted 16th March 2026

DOI: 10.1039/d6ra00367b

[rsc.li/rsc-advances](http://rsc.li/rsc-advances)

## 1 Introduction

Nanoscience has become a focal point in contemporary materials study, which assists in the design and control of matter at the nanoscale to obtain qualities that cannot be obtained in bulk systems. Advances have been made in energy storage, catalysis, and environmental technologies due to the characteristic properties of nanostructured materials, such as high surface-area-to-volume ratios, high interfacial energy and the quantum confinement effect.<sup>1,2</sup>

Among the various categories of nanomaterials, inorganic nanoparticles are considered one of the most interesting due to their thermal and chemical stability, structural rigidity and adjustable physicochemical properties. The size, shape and structure of particles can be controlled to precisely modulate their properties, which directly affect catalytic efficiency, optical activity and mechanical performance.<sup>3,4</sup> As a result, recent advances in synthesis methods have been oriented towards the use of methods that are more morphologically precise and

environmentally sustainable. These strategies aim at curbing chemical hazards and minimizing energy consumption through the use of renewable raw materials and thus help in the shift towards cleaner and greener pathways for the synthesis of nanomaterials.<sup>5,6</sup>

Various techniques have been developed to fabricate nanoparticles, which are typically classified as top-down or bottom-up procedures.<sup>7</sup> Despite their ability to achieve controlled synthesis through physical and chemical methods, their economic and environmental sustainability is low because they often demand high energies, expensive equipment, and toxic substances.<sup>8</sup> Biological techniques involving the use of microorganisms or plant extracts as alternatives are more sustainable in terms of scalability and reproducibility.<sup>9,10</sup> Green synthesis, in turn, is a promising approach that uses mild reaction conditions and renewable precursors to reduce the use of energy and minimize the amount of chemical waste.<sup>11,12</sup> Greenly generated nanoparticles may be more stable and active on their surfaces because of the capping or stabilizing agents that are naturally obtained.<sup>8,13</sup> This green technology is a viable solution for synthesizing silica nanoparticles (SiO<sub>2</sub> NPs) using natural biomass sources in an eco-friendly manner and does not contradict existing trends in the development of sustainable materials. Silica nanoparticles can be shaped in various shapes,

<sup>a</sup>Department of Chemistry, College of Science, University of Sulaimani, Qlisan St, 46001, Sulaymaniyah, Kurdistan Region, Iraq

<sup>b</sup>Department of Physics, College of Science, University of Sulaimani, Qlisan St, 46001, Sulaymaniyah, Kurdistan Region, Iraq. E-mail: omed.abdullah@univsul.edu.iq



including spheres, rods, and plates. Both types of forms have different surface energies and physicochemical properties.<sup>14</sup> The ability to tailor these parameters provides a pathway for optimizing the performance of SiO<sub>2</sub> NPs for particular uses in different industries.<sup>15</sup> Because of their high thermal stability, SiO<sub>2</sub> NPs are also used as reinforcing agents in metal and polymer matrix composites, which can improve the mechanical strength and durability of structural materials.<sup>16</sup>

The synthesis of SiO<sub>2</sub> NPs is highly dependent on the nature of the precursor material used, and as a result, the material selected affects the structure and functional characteristics of that material. Chemical precursors, such as silicon tetrachloride (SiCl<sub>4</sub>), tetraethyl orthosilicate (TEOS) and sodium silicate (Na<sub>2</sub>SiO<sub>3</sub>), have traditionally been the most commonly used precursors, as they are efficient in terms of controlled nanoparticle synthesis but generate hazardous byproducts.<sup>17–21</sup> At the same time, biosynthesized SiO<sub>2</sub> NPs through bacteria, fungi, yeast, plant extracts, or algal biomass constitute an eco-friendly, viable solution to traditional chemical processing.<sup>22–24</sup> The increasing consciousness regarding environmental conservation has led researchers to seek other sources of silica that are more sustainable; accordingly, there have been increased interests in natural renewable sources and silica sources that are industrial wastes, such as wheat husk,<sup>25</sup> coconut husk ash,<sup>26</sup> corn cob ash,<sup>27</sup> rice husk ash,<sup>28,29</sup> lemon grass,<sup>30</sup> sugarcane leaves,<sup>31</sup> St. Augustine grass,<sup>32</sup> sand,<sup>33,34</sup> and mineral rocks.<sup>35–37</sup>

These reserves contain amorphous silica sources and can be used to produce nanoparticles that are sustainable to the environment and have a low environmental impact. Although numerous methods of chemical synthesis have been developed, the large-scale manufacture of nano-silica remains an economically problematic issue because of the high cost of materials and energy-consuming steps of the production process. This has prompted scientists to explore less costly and more readily available natural materials as sustainable alternative sources of silica. Silica nanoparticles are widely used across diverse fields due to their highly adaptable surface chemistry, structural stability, and favorable biocompatibility. Within the clinical and diagnostic sectors, researchers have prioritized silica-based nanomaterials for applications in drug delivery, diagnostic imaging, and theranostic platforms, where the pore structure and surface functionality critically influence performance.<sup>38–40</sup> Consequently, mastering the precision synthesis and structural tailoring of SiO<sub>2</sub> NPs remains a fundamental challenge in optimizing their performance.

The present study develops a cost efficient yet eco-friendly method to prepare SiO<sub>2</sub> NPs through a green precipitation process by utilizing locally available rice husk biomass as a renewable silica source. Three methodologies for controlled ashing were employed to determine the role of processing conditions in the size and shape of NPs. Furthermore, the amorphous-crystalline transition was studied in detail. The structural and morphological characterizations were carried out in a comprehensive manner to explain the relationship between the conditions of processing and material properties. The results reveal that rice husk has the potential to be an effective

and sustainable precursor in the production of large-scale and phase-controlled synthesis of high-purity SiO<sub>2</sub> NPs.

## 2 Experimental parts

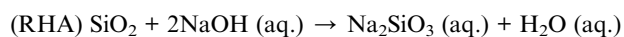
### 2.1 Materials

All the chemical reagents such as sodium hydroxide (NaOH), hydrochloric acid (HCl), and sulfuric acid (H<sub>2</sub>SO<sub>4</sub>) were of analytical grade and purchased from Merck (Germany). The experiments were conducted using double-distilled water. The silica precursor, rice husk (RH), was gathered in an area rice mill (Chwar Bakh rice mill in Sulaymaniyah City).

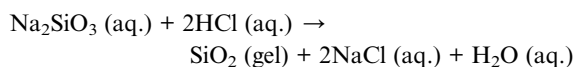
### 2.2 Procedure

Silica nanoparticles (SiO<sub>2</sub> NPs) were prepared from agricultural waste using rice husk waste *via* silica xerogel production. The RH collected at a milling unit was washed twice with running tap water and once more twice with distilled water to clean any dust, flour or contaminants. The dried husk was dried in an oven at 100 ± 5 °C and later placed in airtight containers pending other phases of this research. Three different ashing procedures were employed to convert RH into rice husk ash (RHA), with each process aimed at controlling the oxidizing environment during combustion to a significant degree. In the former method, the material was placed in an open ceramic crucible, burned under normal atmospheric conditions, and left to be completely exposed to oxygen (direct method). The second technique used a partially covered crucible to restrict the oxygen supply, forming a semi-controlled environment that controlled the rate of oxidation (limited O<sub>2</sub>). RH in the third route went through a closed furnace chamber, which was constantly purged with high-purity nitrogen gas (99–99.9%) to create an inert atmosphere (entirely oxygen-free atmosphere) that favored the pyrolytic breakdown of the compound over complete combustion (under N<sub>2</sub>). In all the procedures, all the samples received identical thermal histories and were heated in a muffle furnace at ambient temperatures of 700 °C at a constant heating rate of 10 °C min<sup>-1</sup> and then 700 °C with a holding time of 4 h to ensure full reaction of the RH to white RHA.

The white ash was first milled into fine powder and then sieved using a sieve of 600 μm. Subsequently, 20 g of rice husk ash (RHA) was placed in a conical flask and combined with 200 mL of 2 M NaOH. The suspension was refluxed at 80–90 °C for 2 h using a heating mantle with continuous stirring to extract silica from the RHA in the form of sodium silicate. Stoichiometric proportions of RHA, NaOH, and HCl were used to facilitate silica precipitation. The extraction of silica was followed by two consecutive steps: (i) dissolution in alkali and (ii) precipitation by acid. The first step involved the dissolution of the RHA in strong alkali (NaOH) to dissolve the amorphous silica, which formed an aqueous solution of sodium silicate (Na<sub>2</sub>SiO<sub>3</sub>).



After separation from the solid residue, the alkaline filtrate containing sodium silicate ( $\text{Na}_2\text{SiO}_3$ ) was slowly neutralized with dilute 0.05 N HCl to a final pH of 7. This gradual pH adjustment triggered the acid-driven precipitation step, leading to the formation of a colloidal silica hydrogel.



The neutralization step is very important for enhancing the formation and subsequent polycondensation of the reactive groups of silanol ( $\text{Si-OH}$ ). This sol-gel reaction leads to the development of a three-dimensional Si-O-Si network that characterizes the silica gel structure.<sup>41</sup> The hydrogel slurry formed at the end of the precipitation using an acid underwent further processing to produce the final silica product. The slurry was allowed to age for 30 h to ensure complete gelation and network development, followed by filtration. The collected gel was repeatedly washed using distilled water to remove soluble impurities, particularly NaCl generated during neutralization. The silica gel was then purified and ultrasonicated to disrupt residual agglomerates and enhance the dispersion of the nanoparticles to yield particles in the size range of 20–100 nm. Subsequently, the silica was dried in an oven at a temperature of 110 °C for 12–24 h to dry up the remaining moisture. Fig. 1 depicts a schematic representation of the production process of the  $\text{SiO}_2$  NPs. A portion of the dried silica was sintered at 1000 °C in a muffle furnace to promote densification and crystallization for structural evaluation. Finally, the process efficiency was assessed by calculating the percentage recovery of RHA and the extracted silica using the following equations:

$$\% \text{RHA recovery} = \frac{\text{Amount of RHA recovered}}{\text{Starting amount of RH}} \times 100, \quad (1)$$

$$\% \text{Silica recovery} = \frac{\text{Mass of the silica recovered}}{\text{Starting mass of RHA}} \times 100. \quad (2)$$

The calculated data were organized, as presented in Table 1. These results highlight the importance of the oxidation environment on the mass yield of rice husk ash (RHA) and silica recovery efficiency. The highest RHA yield (39.1%) was obtained with ashing under  $\text{N}_2$  atmosphere, and it can be attributed to restricted oxygen availability that promotes pyrolytic degradation of organic matter and minimizes mass loss. However, silica recovery from this ash was the lowest (40.2%), indicating that the resulting ash structure exhibits reduced chemical reactivity. Conversely, direct ashing under ambient oxygen conditions produced the highest silica recovery efficiency (98.1%), with moderate RHA recovery (28.7%). This suggests that complete oxidation enhances the accessibility and reactivity of silica, thereby improving its subsequent chemical extraction. Therefore, maximizing the overall silica yield requires prioritizing extractability (high silica recovery) over the raw mass recovered from the initial ashing step. The reduced silica recovery observed under limited  $\text{O}_2$  and  $\text{N}_2$  atmospheres can be attributed to incomplete oxidation of carbonaceous species, resulting in carbon-rich residues that limit silica extractability. In contrast, the direct method maximizes silica yield per unit

Table 1 Recovery percentages of RHA and extracted silica

| Ashing methods | % RHA recovery | % Silica recovery |
|----------------|----------------|-------------------|
| Direct         | 28.7           | 98.1              |
| Limited oxygen | 25.8           | 58.6              |
| Under nitrogen | 39.1           | 40.2              |

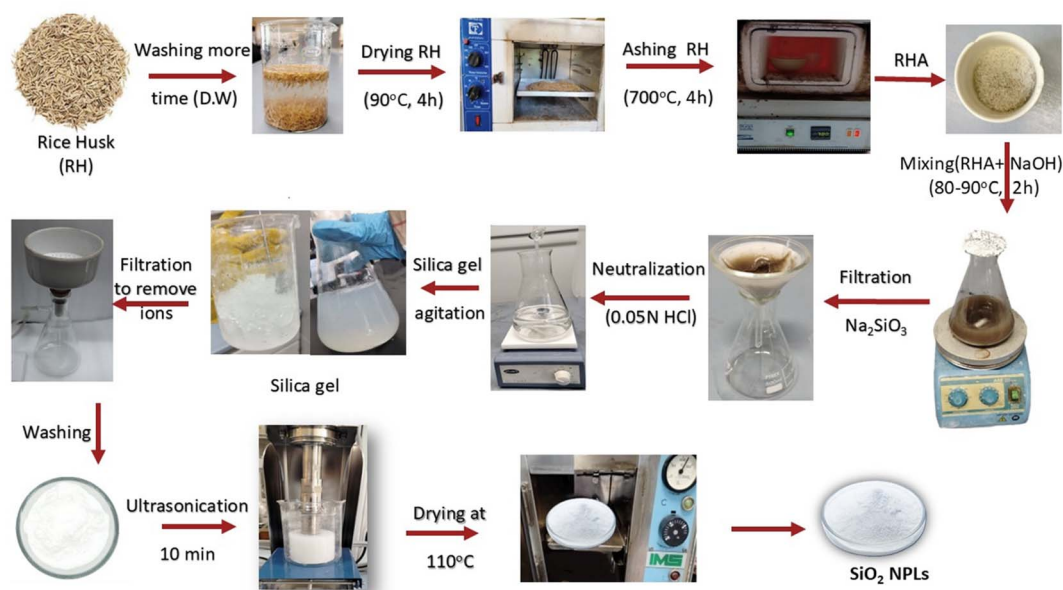


Fig. 1 Schematic of the thermo-chemical and post-processing routes in the production of silica nanoparticles from RH.



precursor and avoids the need for controlled atmospheres, thereby reducing operational complexity, energy demand, and associated emissions. Thus, direct calcination represents a more resource-efficient and comparatively lower process-burden pathway for silica extraction than the limited O<sub>2</sub> and under N<sub>2</sub> atmosphere.

### 2.3 Characterization techniques

Fourier-transform infrared (FTIR) spectroscopy was applied to monitor the chemical bonds present in the SiO<sub>2</sub> NPs and to confirm the removal of organic residues. The analysis was conducted using a PerkinElmer spectrometer (Model 2000) and Thermo Scientific Nicolet (Model: iS10), over the wavenumber range of 400–4000 cm<sup>-1</sup>. Prior to measurement, the specimens were mixed with spectroscopic-grade potassium bromide (KBr) and pressed into transparent pellets across the relevant vibrational range.

X-ray diffraction (XRD) measurements were conducted using a Philips-PW1730 diffractometer equipped with a Cu anode ( $\lambda = 0.154$  nm) operated at a maximum power of 2.2 kW and a voltage of 60 kV. The system utilized a long fine-focus ceramic tube, and diffraction patterns were recorded within a  $2\theta$  range of 10°–80° with a constant scan rate of 5° min<sup>-1</sup>. These data were used to determine the crystalline phase of the prepared SiO<sub>2</sub> NPs and to estimate their average crystallite size.

A field emission-scanning electron microscope (FE-SEM) was used to assess the surface morphology of the prepared SiO<sub>2</sub> NPs; microstructural imaging was conducted using a TESCAN MIRA3 produced in Czechia. Prior to FE-SEM imaging, the samples were sputter-coated with a thin gold layer to enhance electrical conductivity and minimize charging effects, thereby ensuring stable, high-contrast micrographs. Elemental analysis was conducted using energy-dispersive X-ray spectroscopy (EDX) integrated within the FE-SEM system. High-resolution FE-SEM images were first acquired to identify regions of interest for elemental mapping. EDX software was subsequently employed to generate color-coded elemental maps illustrating the surface distribution of the constituent elements. Transmission electron microscopy (TEM) analysis was performed using a PHILIPS CM120 microscope to investigate the morphology and particle size distribution of the SiO<sub>2</sub> NPs. For TEM analysis, a small amount of the SiO<sub>2</sub> powder was ultrasonically dispersed in alcohol, and a drop of the suspension was deposited onto a carbon-coated copper grid and allowed to dry before imaging.

The zeta potential of synthesized SiO<sub>2</sub> NPs using different ashing methods was measured by dispersing the nanoparticles in deionized water. Zeta potential measurements were performed using a Malvern Zetasizer Nano instrument at 25 °C.

The specific surface area (SSA) of the synthesized SiO<sub>2</sub> NPs was estimated using the methylene blue (MB) adsorption method. In this method, a known mass of SiO<sub>2</sub> (0.1 g) was dispersed in an aqueous solution of MB and stirred for 30–60 min until the adsorption equilibrium was reached. The decrease in dye concentration was determined by UV-Vis spectrophotometry at 664 nm. The amount of adsorbed MB was calculated. Assuming monolayer adsorption of MB molecules

on the particle surface, the SSA was estimated from the quantity of MB adsorbed and the known molecular cross-sectional area. This method provides a practical indirect estimation of SSA.

## 3 Results and discussion

### 3.1 FTIR analysis

The FTIR spectra of the SiO<sub>2</sub> NP powder produced from rice husk using different ashing methods are presented in Fig. 2. The three FTIR spectra of silica samples generally exhibit a broad absorption band around 3466 cm<sup>-1</sup>, which corresponds to the O–H stretching vibration of silanol (Si–OH) groups and physically adsorbed water molecules on the silica surface.<sup>27,31</sup> A characteristic peak near 1641 cm<sup>-1</sup> is consistently observed, which is attributed to the bending vibration of water molecules either trapped within the silica matrix or associated with Si–OH groups.<sup>42,43</sup> These features confirm the presence of hydroxyl functionalities and adsorbed water as inherent characteristics of silica materials.

A vigorous peak at 1112 cm<sup>-1</sup> was linked to the stretching asymmetric vibration of Si–O–Si; the stretching symmetric vibration of Si–O–Si was related to the band of 801 cm<sup>-1</sup>, and the band of 468 cm<sup>-1</sup> was attributed to the bending vibration of Si–O in siloxane networks.<sup>42</sup>

The enhanced Si–O–Si bending vibration band observed in the limited O<sub>2</sub> sample can be attributed to modified combustion kinetics during the ashing process. Reduced oxygen availability moderates oxidation, enabling gradual silanol (Si–OH) condensation and promoting the development of a more interconnected siloxane (Si–O–Si) network.<sup>44</sup> In contrast, fully oxidative conditions may induce rapid combustion and localized thermal effects, which can alter bond distribution within the silica framework. Compared with N<sub>2</sub> treatment, limited O<sub>2</sub> provides sufficient oxidative conditions to facilitate silanol condensation while limiting excessive structural damage. Consequently, the resulting higher degree of siloxane cross-linking is reflected in the increased intensity of the Si–O–Si bending vibration.

The band observed near 618 cm<sup>-1</sup> is commonly assigned to the rocking lattice vibration modes of SiO<sub>2</sub> cristobalite, resulting from the Si–O–Si framework's rocking vibrations in the ordered tetrahedral network.<sup>45</sup> The presence of this band in all three samples is therefore considered a spectroscopic indicator of crystalline silica with domains of the cristobalite phase after sintering at high temperatures. The chemical purity of the synthesized silica was also supported by the absence of impurity bands in the range of 1700–2750 cm<sup>-1</sup>. Furthermore, the small band at 975 cm<sup>-1</sup> in all silica samples, which was assigned to the silanol groups, represented a slight deviation from the commercial silica spectra. The synthesis of silanol and siloxane groups can be associated with the process of hydrolysis and condensation of the acid-neutralized solubilization of sodium silicate. In general, the FTIR spectra support the similarity between the structures of all three derived silicas using different ashing methods. These spectral features confirmed the purity of the synthesized silica using different ashing methods. Table 2



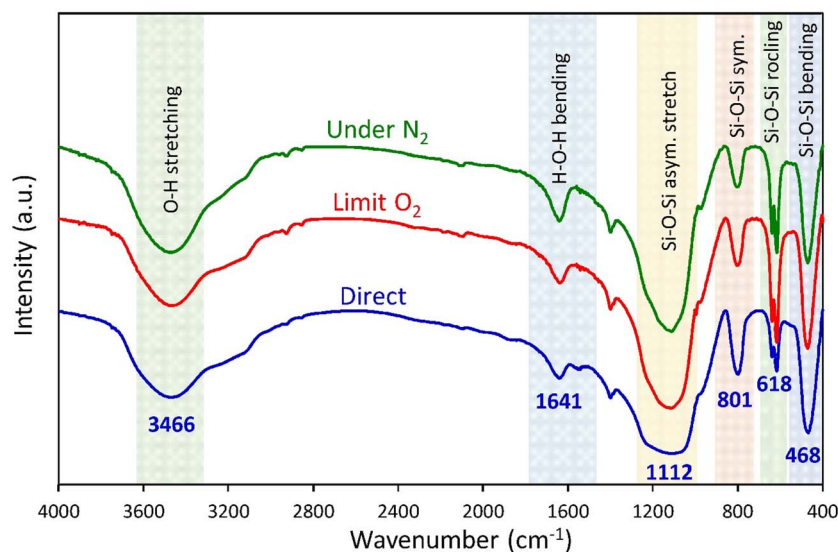


Fig. 2 FTIR spectra of the SiO<sub>2</sub> NP powder synthesized from RH using different ashing methods.

Table 2 FTIR spectra bands for the synthesized SiO<sub>2</sub> NPs using the direct ashing method

| Wavenumber (cm <sup>-1</sup> ) | Vibration type        | Assignment                      | Structural meaning                      |
|--------------------------------|-----------------------|---------------------------------|---|
| 3466                           | O–H stretching        | Si–OH/adsorbed H <sub>2</sub> O | Surface hydroxyl group                  |
| 1641                           | H–O–H bending         | H <sub>2</sub> O molecule       | Adsorbed water                          |
| 1112                           | Si–O–Si asym. stretch | Siloxane bond                   | SiO <sub>2</sub> network                |
| 801                            | Si–O–Si sym. stretch  | Siloxane                        | Tetrahedral structure                   |
| 618                            | Si–O–Si rocking       | Siloxane                        | Cristobalite SiO <sub>2</sub> framework |
| 468                            | Si–O–Si bending       | Siloxane                        | Amorphous SiO <sub>2</sub> framework    |

summarizes the important FTIR vibrational modes of as-synthesized SiO<sub>2</sub> NPs.

### 3.2 XRD analysis

The structural features of the synthesized SiO<sub>2</sub> NPs from RH through different approaches, including direct ashing, limited O<sub>2</sub> and under N<sub>2</sub> atmosphere, were examined using XRD, as depicted in Fig. 3. The XRD patterns of all samples exhibited a single broad diffraction halo, characteristic of amorphous silica dried at 110 °C, confirming the absence of sharp diffraction peaks associated with crystalline phases or impurities. The position of this broad peak reflects the most probable inter-atomic correlation distance within the amorphous structure. The shift of this amorphous maximum from 21.69° to 22.98° and 23.26° for synthesized SiO<sub>2</sub> NPs *via* direct, under N<sub>2</sub>, and limited O<sub>2</sub> atmosphere, respectively, indicates a systematic reduction in mean inter-atomic spacing, which is consistent with denser local packing. The concurrent intensity loss and peak broadening suggest reduced short-range structural coherence and a higher level of structural disorder.<sup>43,46</sup>

The XRD patterns of SiO<sub>2</sub> NP powder after sintering at 1000 °C are presented in Fig. 4, revealing a clear transition from the initially amorphous SiO<sub>2</sub> NP structure to a crystalline phase. Sintering of SiO<sub>2</sub> NPs powder prepared by direct ashing induces

the emergence of multiple sharp diffraction peaks at  $2\theta = 22.1^\circ$ ,  $28.5^\circ$ ,  $31.6^\circ$ ,  $36.2^\circ$ ,  $36.6^\circ$ ,  $42.8^\circ$ ,  $45.1^\circ$ ,  $47.3^\circ$ ,  $48.8^\circ$ ,  $54.5^\circ$ ,  $57.3^\circ$ ,  $60.6^\circ$ ,  $62.3^\circ$ ,  $65.4^\circ$ ,  $69.1^\circ$ ,  $73.1^\circ$ , and  $74.3^\circ$ , confirming the development of a long-range order. These diffractions are attributed to crystalline phase planes (011), (111), (012), (020), (112), (121), (022), (113), (122), (023), (031), (131), (032), (132), (124), (133) and (232) of a crystalline tetragonal SiO<sub>2</sub> cristobalite phase, with cell parameters  $a = b = 4.95 \text{ \AA}$  and  $c = 6.876 \text{ \AA}$ , in agreement with the reference pattern PDF Code 96-900-1580.<sup>9,47</sup> Therefore, the XRD results show that the as-extracted amorphous silica is converted into well-crystallized silica through the process of sintering for all SiO<sub>2</sub> NP powders synthesized from RH using different ashing methods. At high temperatures (1000 °C), the thermal energy is sufficient to promote bond rearrangement, enabling atomic diffusion and reorganization of coordination units and the nucleation and growth of stable crystalline domains. As these nuclei grow, they replace the short-range order of the amorphous SiO<sub>2</sub> NPs with extended lattice structures, giving rise to increasingly sharp and intense Bragg reflections. The purity of the synthesized SiO<sub>2</sub> NPs is further affirmed by the absence of extraneous peaks, indicating that the dominant phase is silica. Such amorphous silica and crystalline silica, due to their high surface area and reactivity, are considered highly valuable for a wide range of industrial and environmental applications.<sup>48</sup>



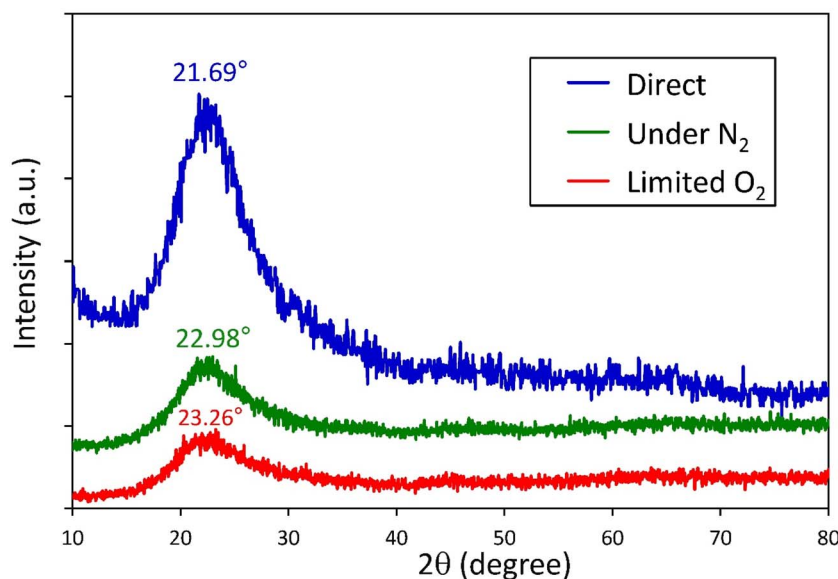


Fig. 3 XRD patterns of the SiO<sub>2</sub> NP powder synthesized from RH using different ashing methods.

It is clear from Fig. 4 that the sample produced by direct ashing crystallized into a single tetragonal cristobalite phase, indicating that its precursor mixture followed a uniform decomposition and nucleation pathway. The SiO<sub>2</sub> NPs prepared under N<sub>2</sub> and limited O<sub>2</sub> atmosphere after sintering at 1000 °C crystallized into polymorphs of α-cristobalite (PDF Code: 96-900-1580) with tridymite (PDF Code: 96-901-3394) or quartz (PDF Code: 96-900-9667).<sup>49</sup> It is important to note that the SiO<sub>2</sub> NP product formed during the direct-ashing process crystallized predominantly into a single cristobalite phase, while the product formed by the limited O<sub>2</sub> ashing process consisted of two crystalline cristobalite and quartz phases. However, the existence of the cristobalite and tridymite phases was predominant in ashing in a nitrogen atmosphere.<sup>50</sup> Although the crystallization pathways differ for different ashing methods, the absence of extraneous peaks confirms that all samples remain compositionally pure. However, prepared SiO<sub>2</sub> NPs under N<sub>2</sub> and limited O<sub>2</sub> atmosphere yielded two polymorphic forms rather than impurity-driven phases.

The formation of a single dominant phase in the direct-ashing process and two phases in limited O<sub>2</sub> and under N<sub>2</sub> conditions can be attributed to atmosphere-dependent crystallization kinetics. Excess oxygen promotes the rapid and homogeneous combustion of organic residues, resulting in a structurally homogenous amorphous precursor that primarily crystallizes as a single cristobalite phase. However, restricted oxygen availability slows down decomposition, alters defect distribution within the silica network, and increases structural heterogeneity. These factors alter nucleation and growth kinetics during sintering, enabling competitive phase development and the coexistence of secondary crystalline phases. Thus, according to the present results, oxygen control is one of the major parameters in tailoring structural and recovery outcomes.

To assess the influence of the three ashing methods on the structural coherence of the resulting SiO<sub>2</sub> NPs, the crystallite dimensions were estimated using the Scherrer formula:

$$D = \frac{k\lambda}{\beta \cos \theta} \quad (3)$$

where  $D$  is the mean crystallite size,  $k$  is the shape factor constant typically taken as 0.9,  $\lambda$  is the X-ray wavelength ( $\lambda = 1.5406 \text{ \AA}$ ),  $\beta$  is the full width at half maximum (FWHM) of the selected diffraction peak, and  $\theta$  is the corresponding Bragg angle. The application of this analysis revealed notable differences among the ashing methods. The SiO<sub>2</sub> NPs produced using the direct ashing method exhibited an average crystallite size of approximately 11.48 nm, while limited O<sub>2</sub> and under N<sub>2</sub> atmosphere ashing yielded markedly larger values of about 25.78 nm and 32.78 nm, respectively. This systematic increase indicates that the thermal and chemical conditions inherent to each ashing route govern the extent of crystallite coarsening during nucleation and growth. The differences in crystallite size among the three ashing routes indicate that the atmosphere of ashing adjustment is an effective lever for tuning the crystallinity of the resulting SiO<sub>2</sub> NPs.

### 3.3 FE-SEM and EDX analyses

FE-SEM observations confirmed that the SiO<sub>2</sub> NPs produced through the green synthesis processes using agro-wastes (RH) possessed a predominantly spherical morphology and nanoscale dimensions, with their particle sizes varying systematically according to the specific ashing method used. The FE-SEM micrographs of the SiO<sub>2</sub> NPs obtained from direct, under N<sub>2</sub> atmosphere, and limited O<sub>2</sub> ashing methods are shown in Fig. 5. In all cases, the particles exhibit limited aggregation, forming small clusters while largely retaining their individual morphology. This mild agglomeration is typical of nanoscale ceramics and arises from surface-driven interactions during drying and powder handling.<sup>51</sup> The partial aggregation observed in the green-synthesized SiO<sub>2</sub> NPs is anticipated because of their large surface area, and the resulting attractions between nanoparticles promote the formation of small asymmetrical



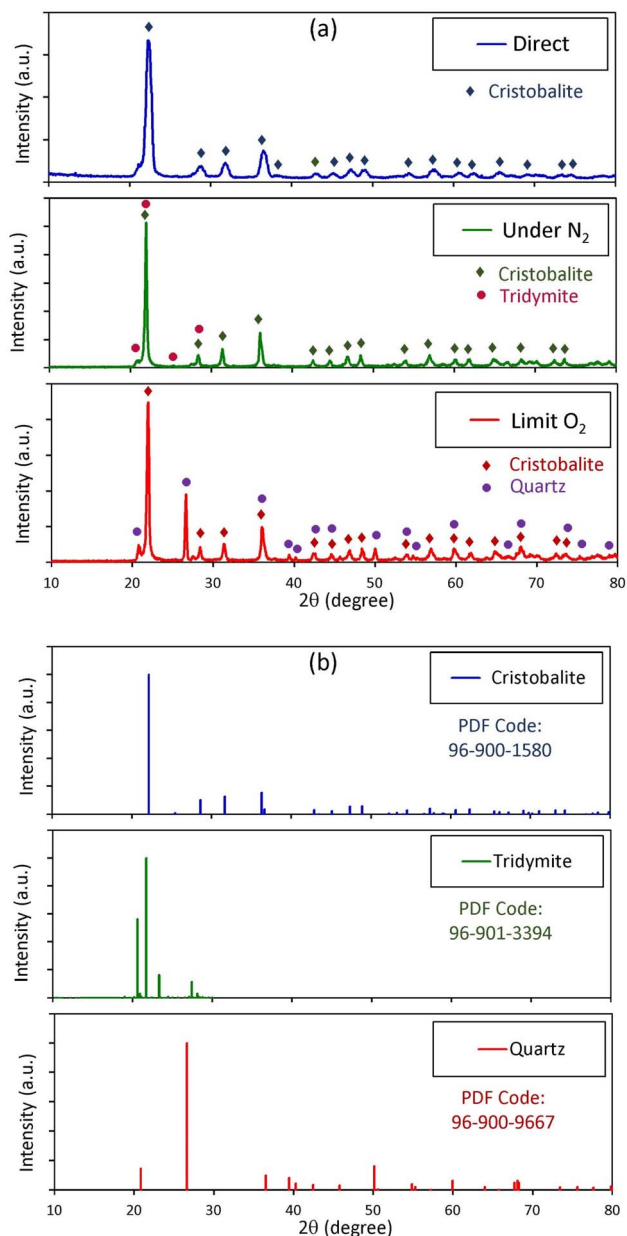


Fig. 4 XRD pattern of the (a) SiO<sub>2</sub> NP powder synthesized from RH using different ashing methods after sintering at 1000 °C and (b) standard reference pattern of the cristobalite, tridymite, and quartz phases.

clusters. In agro-waste extracts, the abundance of a large fraction of hydroxyl-bearing organic molecules tends to slow down condensation and hydrolysis reactions, thereby restricting particle growth and reducing the formation of oversized particles. In addition, the diverse phytochemicals present in the extracts act as stabilizing and capping agents, influencing both the stability and aggregation properties of the nanoparticles. These observations underline that the chemical profile of the extract, as well as dispersion conditions during synthesis, play a crucial role in determining nanoparticle size, morphology, and colloidal behavior.<sup>52</sup>

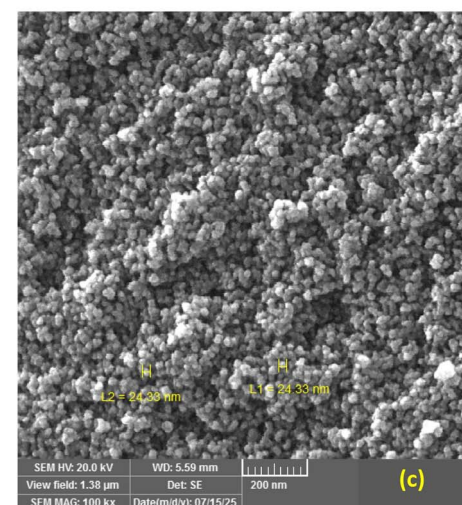
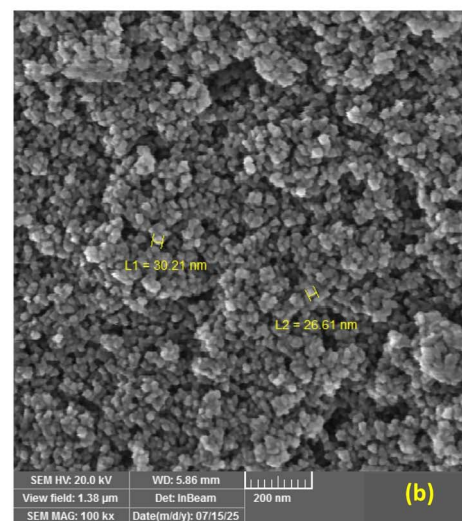
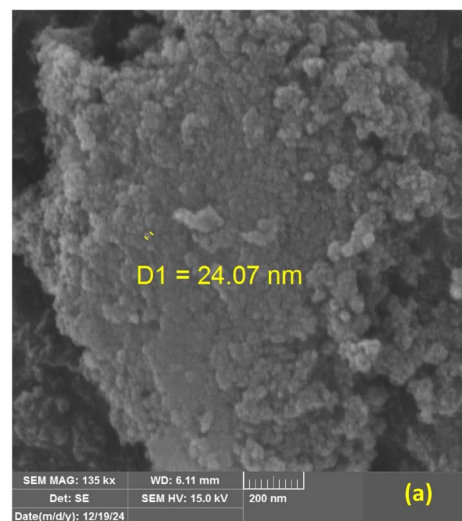


Fig. 5 FE-SEM images of the SiO<sub>2</sub> NP powder synthesized from RH using different ashing methods: (a) direct, (b) limited oxygen, and (c) under nitrogen.



The chemical composition of SiO<sub>2</sub> NP powder extracted from RH using different ashing methods was determined using EDX spectroscopy, as shown in Fig. 6. EDX results confirmed that the as-prepared SiO<sub>2</sub> NPs using the three ashing methods, direct, limited O<sub>2</sub>, and under N<sub>2</sub> atmosphere, exhibit high elemental purity. In all samples, the SiO<sub>2</sub> signal dominated the spectrum, corresponding to a purity level exceeding 98 wt%. Minor signals associated with trace elements were also detected; these are attributed either to residual precursors or to unavoidable background contributions from the substrate and coating. The elemental composition of the synthesized SiO<sub>2</sub> NPs using the direct method is summarized in Table 3. Although the samples

**Table 3** Elemental composition of SiO<sub>2</sub> NPs extracted from RH using the direct method

| Elements | O     | Si   | Na   | Mg  | Al   | S    | Cl   | K    | Ca   | Fe   |
|----------|-------|------|------|-----|------|------|------|------|------|------|
| wt%      | 63.33 | 34.7 | 0.21 | 0.0 | 0.19 | 0.14 | 0.04 | 0.09 | 0.21 | 0.11 |

exhibit high purity SiO<sub>2</sub>, small amounts of residual impurities were still detectable after the extraction. The close similarity of the EDX profiles across the three ashing approaches indicates that the ashing atmosphere does not markedly influence the elemental composition and that all methods yield SiO<sub>2</sub> NPs with comparable chemical cleanliness. EDS analysis confirmed that silica constituted the primary phase across all samples. The calculated atomic ratios of Si : O for the three prepared, direct, limited O<sub>2</sub>, and under N<sub>2</sub> are 1 : 2.82, 1 : 2.33, and 1 : 1.24, respectively. Although the first two methods yielded oxygen levels slightly exceeding the theoretical stoichiometric ratio of 1 : 2, the third method resulted in a sub-stoichiometric oxygen content. The elevated oxygen values in the direct and limited O<sub>2</sub> samples are likely due to the common overestimation of oxygen in EDS measurements, as well as the presence of surface hydroxyl groups in silica materials, which is consistent with our earlier FTIR analysis. Conversely, the oxygen deficiency observed in the under N<sub>2</sub> sample can be attributed to the inert synthesis atmosphere, which significantly limited the O<sub>2</sub> availability during the ashing method.

### 3.4 TEM analysis

TEM was employed to visualize the morphology and size of the synthesized SiO<sub>2</sub> NPs extracted from RH through different ashing routes, while particle-size distributions were obtained by determining representative particles in ImageJ. The TEM micrographs of SiO<sub>2</sub> NPs extracted from RH through different ashing routes are presented in Fig. 7. The particle-size distributions derived from the TEM image analysis are depicted in Fig. 8. The obtained results reveal clear variances in nanoparticle size and dispersion according to the ashing methods. The histograms show a progressive shift toward larger SiO<sub>2</sub> NP sizes upon shifting from the direct ashing method to the ashing method in an N<sub>2</sub> atmosphere. The SiO<sub>2</sub> NPs obtained using the direct ashing method are generally the smallest and exhibit a more uniform appearance with an average diameter close to 20 nm, while the limited O<sub>2</sub> method yields slightly larger nanoparticles with a broader spread in SiO<sub>2</sub> NP size with an average diameter close to 34 nm. Ashing under N<sub>2</sub> atmosphere produces the largest SiO<sub>2</sub> NPs among the three sets (37 nm), and a greater degree of size variation. The observed particle-size distributions obtained using the direct ashing method are consistent with earlier reports on synthesized SiO<sub>2</sub> NPs from fly ash<sup>53</sup> and porous volcanic rock,<sup>54</sup> exhibiting comparable morphology and size characteristics. It is noteworthy that the TEM-derived particle sizes across the three ashing processes exhibit the same growing trend as the crystallite sizes calculated from the XRD data. This consistency between morphological and structural tests supports the synthesis pathway's impact on the formation of SiO<sub>2</sub> NPs.

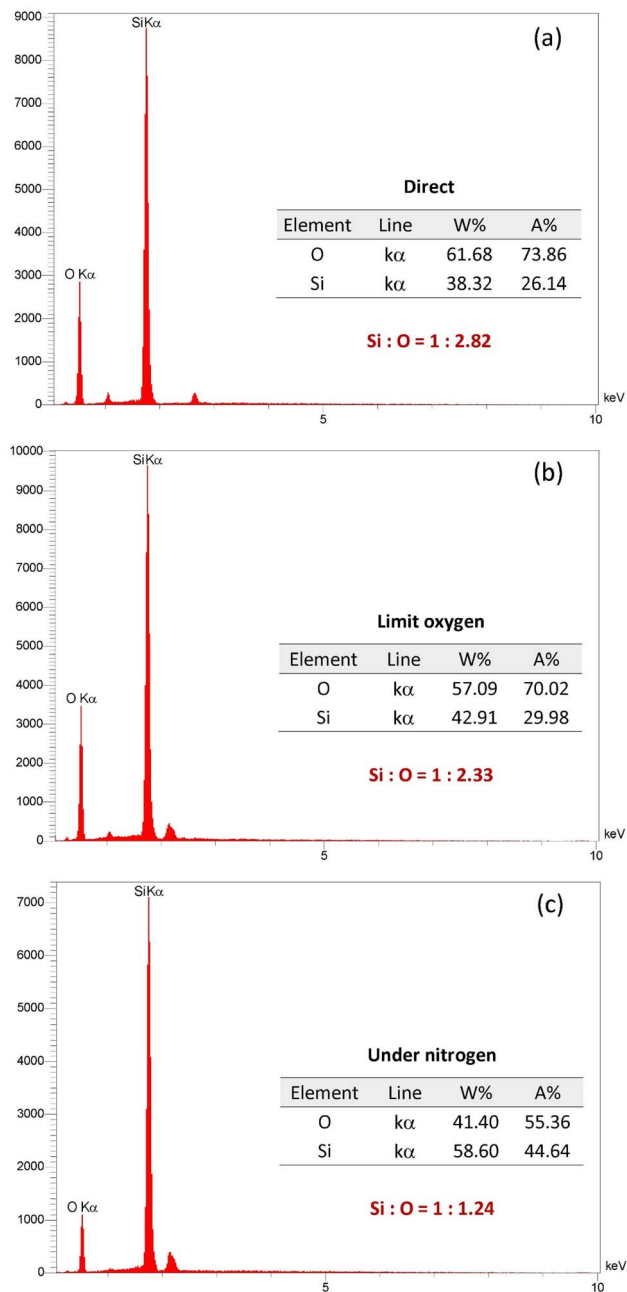


**Fig. 6** Chemical composition of SiO<sub>2</sub> NPs extracted from RH using different ashing methods: (a) direct, (b) limited oxygen, and (c) under nitrogen.



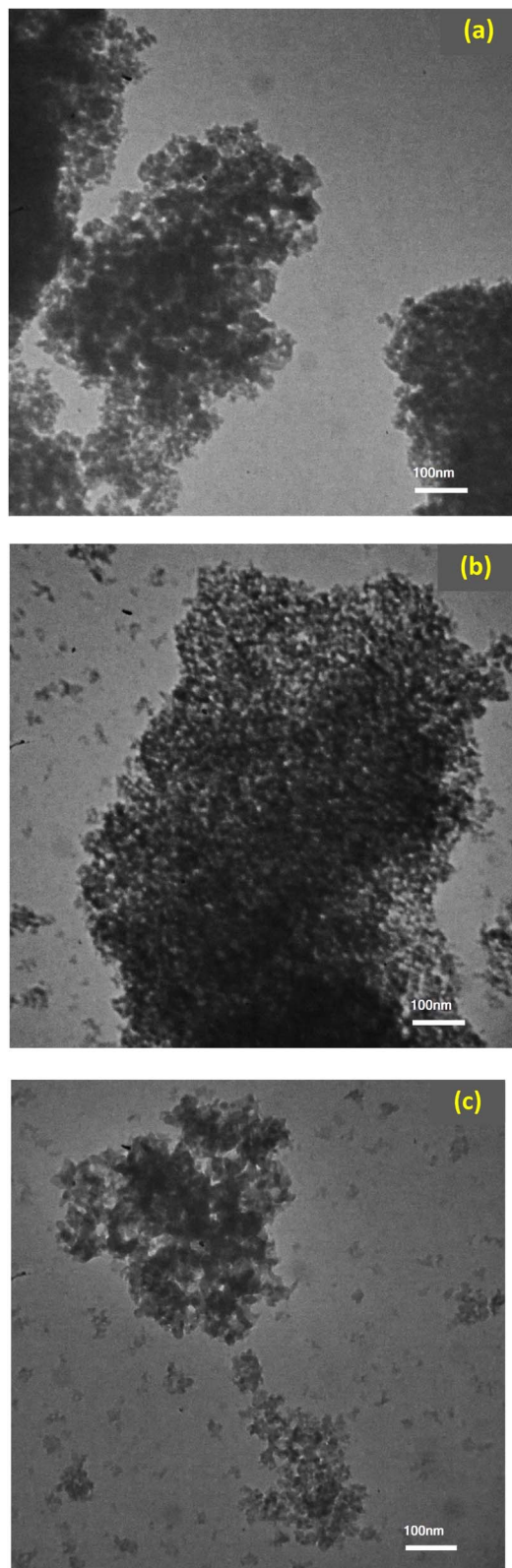


Fig. 7 TEM images of SiO<sub>2</sub> NPs extracted from RH using different ashing methods: (a) direct, (b) limited oxygen, and (c) under nitrogen.

### 3.5 Zeta potential analysis

Zeta potential was measured to assess the electrostatic stability and aggregation tendency of the synthesized SiO<sub>2</sub> NPs, which

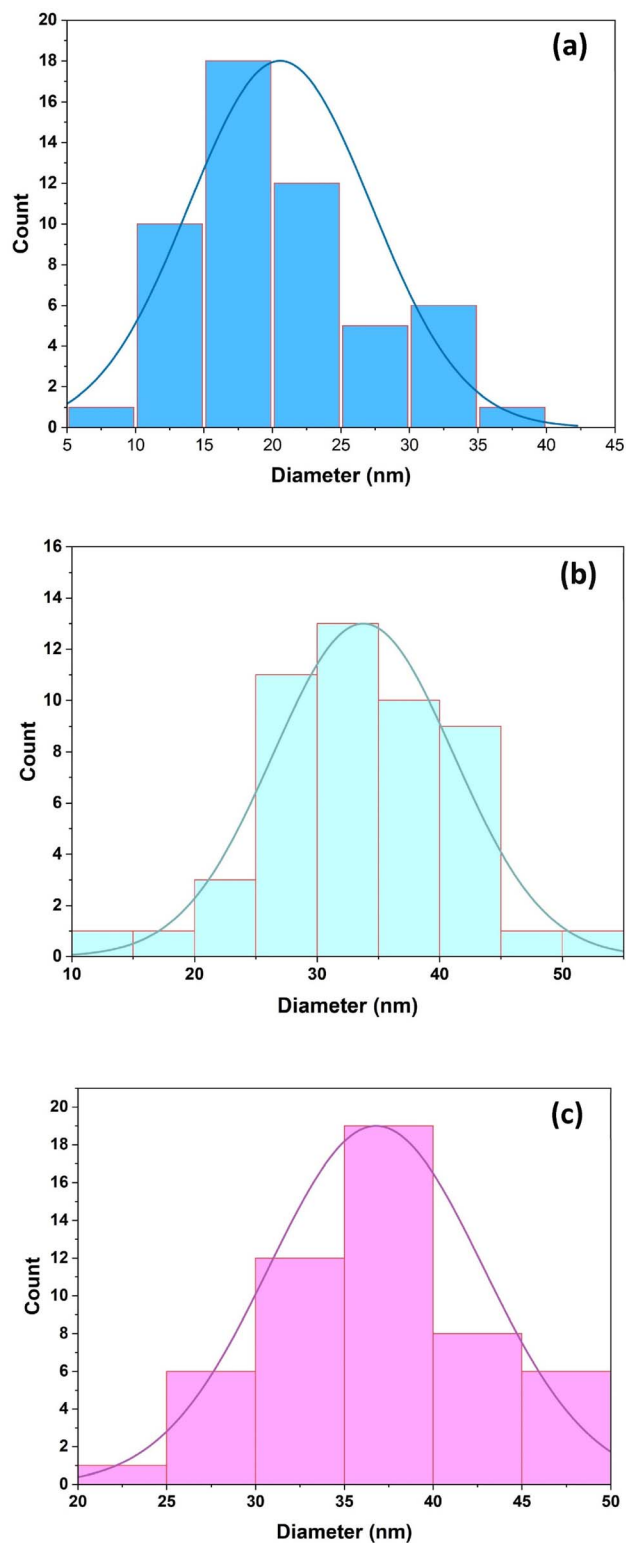


Fig. 8 Particle size distribution of SiO<sub>2</sub> NPs extracted from RH using different ashing methods: (a) direct, (b) limited oxygen, and (c) under nitrogen.

directly influence dispersion homogeneity and subsequent processing behaviour.<sup>52,55</sup> Fig. 9 presents the zeta potential measurements of SiO<sub>2</sub> NPs in deionized water. The zeta



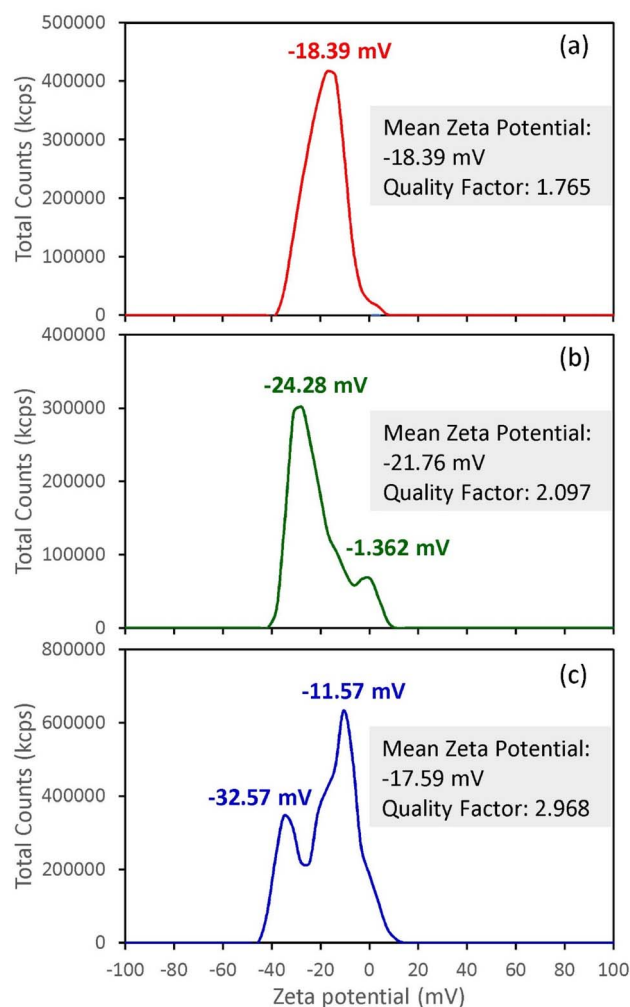


Fig. 9 Zeta potential of SiO<sub>2</sub> NPs extracted from RH using different ashing methods: (a) direct, (b) limited oxygen, and (c) under nitrogen.

potential values for all the syntheses SiO<sub>2</sub> NPs were negative, consistent with previous studies, which have shown that SiO<sub>2</sub> exhibits a negative surface charge under neutral conditions, indicating colloidal stability in aqueous dispersions.<sup>56,57</sup>

Zeta potential measurements revealed a negative surface charge of  $-18.39$  mV for the direct ashing method SiO<sub>2</sub> NPs dispersed in water, indicating moderate electrostatic stability due to the deprotonated Si–OH groups, as confirmed previously in the FTIR analysis section. The unimodal distribution confirms a homogeneous surface charge without evidence of secondary aggregation. The slightly less negative zeta potential compared to amorphous silica is caused by the crystalline phase of the prepared SiO<sub>2</sub> NPs. However, the zeta potential distribution exhibited a bimodal profile with two peaks centered at  $-24.28$  mV and  $-1.362$  mV for ashing with limited O<sub>2</sub>, and  $-32.57$  mV and  $-11.57$  mV for ashing under N<sub>2</sub>, indicating the presence of two electrokinetically distinct nanoparticle populations. The more negative population in the two methods corresponds to well-dispersed SiO<sub>2</sub> NPs exhibiting good electrostatic stability, while the secondary population at less

Table 4 Specific surface area (SSA) of the as-prepared SiO<sub>2</sub> NPs and after sintering at 1000 °C

| Ashing methods | SSA of the as-prepared sample (m <sup>2</sup> g <sup>-1</sup> ) | SSA after sintering (m <sup>2</sup> g <sup>-1</sup> ) |
|----------------|---|---|
| Direct         | 117.40  | 14.71   |
| Limited oxygen | 116.69  | 13.83   |
| Under nitrogen | 115.48  | 13.46   |

negative potentials suggests partially aggregated or weakly charged clusters. These results agree well with the TEM results, where the direct ashing method showed the smallest SiO<sub>2</sub> NPs, while ashing under nitrogen showed a maximum nano size, indicating the aggregation of SiO<sub>2</sub> NPs in this ashing method.

### 3.6 Specific surface area analysis

The specific surface area (SSA) of as-synthesized SiO<sub>2</sub> NPs using different ashing methods and after sintering at 1000 °C was estimated using the MB adsorption method, a widely used approach for evaluating the surface area of porous powders and nanostructured materials.<sup>58</sup> The SSA values for as-synthesized SiO<sub>2</sub> NPs using different ashing methods are presented in Table 4. The calculated values of SSA were 117.40, 116.69, and 115.48 m<sup>2</sup> g<sup>-1</sup> for amorphous silica obtained by direct, limited oxygen, and nitrogen atmosphere ashing methods, respectively, corresponding to MB adsorption values of  $1.500 \times 10^{-5}$ ,  $1.491 \times 10^{-5}$ , and  $1.475 \times 10^{-5}$  mol. These results are in good agreement with other published results for amorphous SiO<sub>2</sub> NPs prepared using different methods.<sup>59,60</sup>

After sintering at 1000 °C, the SSA values of SiO<sub>2</sub> powder significantly decreased to 14.71, 13.83, and 13.46 m<sup>2</sup> g<sup>-1</sup>, with corresponding MB adsorption values of  $1.880 \times 10^{-6}$ ,  $1.768 \times 10^{-6}$ , and  $1.720 \times 10^{-6}$  mol, respectively. The pronounced decrease in the surface area of SiO<sub>2</sub> NPs after sintering can be explained by transforming the amorphous phase into crystalline phases, usually cristobalite, along with sintering, pores collapse and condensation of surface silanol groups at high temperatures. These observations are consistent with the structural features revealed by the XRD and TEM analyses of the samples.

Thus, crystallization caused densification of the silica framework and a decrease in SSA. The results generally reveal that the surface areas of amorphous SiO<sub>2</sub> NPs are much larger than those of their crystalline counterparts, which are formed through high-temperature sintering. The use of a sustainable method with a different ashing approach and sintering enabled the successful synthesis of high-purity SiO<sub>2</sub> NPs from rice husk with a wide range of specific surface areas from 117.40 m<sup>2</sup> g<sup>-1</sup> for amorphous to 13.46 m<sup>2</sup> g<sup>-1</sup> for crystalline phase, indicating its promising potential for applications in catalysis and polymer-based technologies.

## 4 Conclusion

This study demonstrates that ashing environments of agro-waste biomass offer considerable flexibility for tailoring the



characteristics of SiO<sub>2</sub> NPs of comparable purity but distinct size, crystalline phase and morphological features. FTIR spectra confirmed the absence of residual organic groups in all ashing routes and presented a pure SiO<sub>2</sub> NPs powder. XRD analysis confirmed that the as-prepared powders maintained an amorphous nature. However, sintering at 1000 °C produced different structural results, producing a single tetragonal cristobalite phase for the sample prepared using the direct ashing method, and mixed phases with dominant cristobalite in a limited oxygen and nitrogen atmosphere during ashing procedures. The impact of the ashing conditions was further demonstrated by microscopy findings. SEM and TEM revealed noticeable differences in particle size and dispersion. The direct ashing method produced the smallest and most uniform particles; however, the limited oxygen and under nitrogen ashing methods showed progressively larger and more heterogeneous dispersions. These trends were corroborated by the particle-size distributions derived from ImageJ analysis. EDX confirmed high elemental purity across all samples, with very few trace signals. The findings indicate that the ashing condition of the agro-waste extraction process has a significant impact on particle size, morphology, specific surface area and phase development, highlighting the necessity of carefully controlling synthesis ashing conditions when customizing high quality SiO<sub>2</sub> NPs for particular applications.

## Author contributions

Fuad Hama Shareef Radha: data curation, formal analysis, investigation, methodology, validation, visualization, writing – original draft, writing – review & editing. Mohammad Tahir Kareem: conceptualization, supervision, validation, visualization, writing – review & editing. Omed Gh. Abdullah: conceptualization, supervision, validation, visualization, writing – review & editing.

## Conflicts of interest

The authors declare no competing financial or personal interests.

## Data availability

The data will be made available by the corresponding author upon request.

## Acknowledgements

The authors gratefully acknowledge the facilities and support provided by the College of Science, University of Sulaimani, for this study.

## References

- 1 G. K. Prashanth, S. Rao, H. S. Lalithamba, N. P. Bhagya, M. M. Swamy, S. R. Yashodha and H. S. Yogananda, Smart nanomaterials for semiconductor applications: Recent

advances in energy storage and biosensing technologies, *Next Mater.*, 2025, **9**, 100964, DOI: [10.1016/j.nxmate.2025.100964](https://doi.org/10.1016/j.nxmate.2025.100964).

- 2 J. K. Patel, A. Patel and D. Bhatia, Introduction to nanomaterials and nanotechnology, *Chapter in Emerging Technologies for Nanoparticle Manufacturing*, Springer, 2021, pp. 3–23. DOI: [10.1007/978-3-030-50703-9\\_1](https://doi.org/10.1007/978-3-030-50703-9_1).
- 3 N. Baig, I. Kammakakam and W. Falath, Nanomaterials: a review of synthesis methods, properties, recent progress, and challenges, *Mater. Adv.*, 2021, **2**, 1821–1871, DOI: [10.1039/D0MA00807A](https://doi.org/10.1039/D0MA00807A).
- 4 J. Singh, T. Dutta, K. H. Kim, M. Rawat, P. Samddar and P. Kumar, 'Green' synthesis of metals and their oxide nanoparticles: applications for environmental remediation, *J. Nanobiotechnol.*, 2018, **16**, 84, DOI: [10.1186/s12951-018-0408-4](https://doi.org/10.1186/s12951-018-0408-4).
- 5 A. I. Osman, Y. Zhang, M. Farghali, A. K. Rashwan, A. S. Eltaweil, E. M. A. El-Monaem, I. M. A. Mohamed, M. M. Badr, I. Ihara, D. W. Rooney and P. S. Yap, Synthesis of green nanoparticles for energy, biomedical, environmental, agricultural, and food applications: A review, *Environ. Chem. Lett.*, 2024, **22**, 841–887, DOI: [10.1007/s10311-023-01682-3](https://doi.org/10.1007/s10311-023-01682-3).
- 6 M. Huston, M. DeBella, M. DiBella and A. Gupta, Green synthesis of nanomaterials, *Nanomater.*, 2021, **11**, 2130, DOI: [10.3390/nano11082130](https://doi.org/10.3390/nano11082130).
- 7 D. Gupta, A. Boora, A. Thakur and T. K. Gupta, Green and sustainable synthesis of nanomaterials: Recent advancements and limitations, *Environ. Res.*, 2023, **231**, 116316, DOI: [10.1016/j.envres.2023.116316](https://doi.org/10.1016/j.envres.2023.116316).
- 8 R. Peng, M. A. Khan and C. L. Liu, Synthesis of silica nanoparticles and their application of dielectric relaxation spectroscopy- a review. Results, *Chem*, 2023, **6**, 101218, DOI: [10.1016/j.rechem.2023.101218](https://doi.org/10.1016/j.rechem.2023.101218).
- 9 D. Eissa, R. H. Hegab, A. A. Shady and Y. H. Kotp, Green synthesis of ZnO, MgO and SiO<sub>2</sub> nanoparticles and its effect on irrigation water, soil properties, and Origanum majorana productivity, *Sci. Rep.*, 2022, **12**, 5780, DOI: [10.1038/s41598-022-09423-2](https://doi.org/10.1038/s41598-022-09423-2).
- 10 B. Mughal, S. Z. J. Zaidi, X. Zhang and S. U. Hassan, Biogenic nanoparticles: Synthesis, characterisation and applications, *Appl. Sci.*, 2021, **11**, 2598, DOI: [10.3390/app11062598](https://doi.org/10.3390/app11062598).
- 11 H. M. Abuzeid, C. M. Julien, L. Zhu and A. M. Hashem, Green synthesis of nanoparticles and their energy storage, environmental, and biomedical applications, *Crystals*, 2023, **13**, 1576, DOI: [10.3390/cryst13111576](https://doi.org/10.3390/cryst13111576).
- 12 D. Kulkarni, R. Sherkar, C. Shirsathe, R. Sonwane, N. Varpe, S. Shelke, M. P. More, S. R. Pardeshi, G. Dhaneshwar, V. Junnuthula and S. Dyawanapelly, Biofabrication of nanoparticles: sources, synthesis, and biomedical applications, *Biotechnol. Bioeng.*, 2023, **11**, 1–26, DOI: [10.3389/fbioe.2023.1159193](https://doi.org/10.3389/fbioe.2023.1159193).
- 13 L. S. Alqarni, M. D. Alghamdi, A. A. Alshahrani and A. M. Nassar, Green nanotechnology: Recent research on bioresource-based nanoparticle synthesis and applications, *J. Chem.*, 2022, **2022**, 4030999, DOI: [10.1155/2022/4030999](https://doi.org/10.1155/2022/4030999).



- 14 I. Khan, K. Saeed and I. Khan, Nanoparticles: Properties, applications and toxicities, *Arab. J. Chem.*, 2019, **12**, 908–931, DOI: [10.1016/j.arabjc.2017.05.011](https://doi.org/10.1016/j.arabjc.2017.05.011).
- 15 P. B. Chouke, T. Shrirame, A. K. Potbhare, A. Mondal, A. R. Chaudhary, S. Mondal, S. R. Thakare, E. Nepovimova, M. Valis, K. Kuca, R. Sharma and R. G. Chaudhary, Bioinspired metal/metal oxide nanoparticles: A road map to potential applications, *Mater. Today Adv.*, 2022, **16**, 100314, DOI: [10.1016/j.mtadv.2022.100314](https://doi.org/10.1016/j.mtadv.2022.100314).
- 16 S. K. Patel and L. Shi, Recent advances in ceramic-reinforced aluminum metal matrix composites: A review, *Alloys*, 2025, **4**, 18, DOI: [10.3390/alloys4030018](https://doi.org/10.3390/alloys4030018).
- 17 Z. Luo, X. Cai, R. Y. Hong, L. S. Wang and W. G. Feng, Preparation of silica nanoparticles using silicon tetrachloride for reinforcement of PU, *Chem. Eng. J.*, 2012, **187**, 357–366, DOI: [10.1016/j.cej.2012.01.098](https://doi.org/10.1016/j.cej.2012.01.098).
- 18 N. Baccile, F. Babonneau, B. Thomas and T. Coradin, Introducing ecodesign in silica sol-gel materials, *J. Mater. Chem.*, 2009, **19**, 8537–8559, DOI: [10.1039/B911123A](https://doi.org/10.1039/B911123A).
- 19 R. Peng, M. A. Khan, J. Wu and Z. Chen, In situ dielectric spectroscopy monitoring of silica nanoparticle synthesis in cationic water-in-oil microemulsions, *Langmuir*, 2022, **38**, 4121–4128, DOI: [10.1021/acs.langmuir.2c00218](https://doi.org/10.1021/acs.langmuir.2c00218).
- 20 P. P. Ghimire and M. Jaroniec, Renaissance of Stöber method for synthesis of colloidal particles: New developments and opportunities 1, *J. Colloid Interface Sci.*, 2020, **584**, 838–865, DOI: [10.1016/j.jcis.2020.10.014](https://doi.org/10.1016/j.jcis.2020.10.014).
- 21 R. Kamila, Ridwan, M. P. M. Akhir, A. Patriati and A. Insani, Synthesis of silica particles through conventional sol-gel and sonochemistry methods and the effect of catalyst, water concentration and sample environment to the particle size, *J. Phys.: Conf. Ser.*, 2022, **2193**, 012044, DOI: [10.1088/1742-6596/2193/1/012044](https://doi.org/10.1088/1742-6596/2193/1/012044).
- 22 H. E. Kaabo, E. Saied, S. E. D. Hassan, H. M. Mahdy and M. H. Sultan, Penicillium oxalicum-mediated the green synthesis of silica nanoparticles: characterization and environmental applications, *Biomass Convers. Biorefin.*, 2025, **15**, 5229–5246, DOI: [10.1007/s13399-024-05350-6](https://doi.org/10.1007/s13399-024-05350-6).
- 23 M. A. Albalawi, A. M. Abdelaziz, M. S. Attia, E. Saied, H. H. Elganzory and A. H. Hashem, Mycosynthesis of silica nanoparticles using aspergillus niger: control of alternaria solani causing early blight disease, induction of innate immunity and reducing of oxidative stress in eggplant, *Antioxidants*, 2022, **11**, 2323, DOI: [10.3390/antiox11122323](https://doi.org/10.3390/antiox11122323).
- 24 H. Zamani, A. Jafari, S. M. Mousavi and E. Darezereshki, Biosynthesis of silica nanoparticle using Saccharomyces cerevisiae and its application on enhanced oil recovery, *J. Pet. Sci. Eng.*, 2020, **190**, 107002, DOI: [10.1016/j.petrol.2020.107002](https://doi.org/10.1016/j.petrol.2020.107002).
- 25 P. Terzioglu, S. Yucel and C. Kus, Review on a novel biosilica source for production of advanced silica-based materials: Wheat husk, *Asia-Pac. J. Chem. Eng.*, 2019, **14**, e2262, DOI: [10.1002/apj.2262](https://doi.org/10.1002/apj.2262).
- 26 M. F. Anuar, Y. W. Fen, M. H. M. Zaid, K. A. Matori and R. E. M. Khaidir, The physical and optical studies of crystalline silica derived from the green synthesis of coconut husk ash, *Appl. Sci.*, 2020, **10**, 2128, DOI: [10.3390/app10062128](https://doi.org/10.3390/app10062128).
- 27 E. A. Okoronkwo, P. E. Imoisili, S. A. Olubayode and S. O. O. Olusunle, Development of silica nanoparticle from corn cob ash, *Adv. Nanoparticles*, 2016, **5**, 135–139, DOI: [10.4236/anp.2016.52015](https://doi.org/10.4236/anp.2016.52015).
- 28 Y. Shen, Rice husk silica derived nanomaterials for sustainable applications, *Renewable Sustainable Energy Rev.*, 2017, **80**, 453–466, DOI: [10.1016/j.rser.2017.05.115](https://doi.org/10.1016/j.rser.2017.05.115).
- 29 D. Shrestha, T. Nayaju, M. R. Kandel, R. R. Pradhananga, C. H. Park and C. S. Kim, Rice husk-derived mesoporous biogenic silica nanoparticles for gravity chromatography, *Heliyon*, 2023, **9**, e15142, DOI: [10.1016/j.heliyon.2023.e15142](https://doi.org/10.1016/j.heliyon.2023.e15142).
- 30 M. Y. Firdaus, H. Osman, H. S. C. Metselaar and A. R. Rozyanty, A simple method for the production of pure crystalline silica from lemon grass, *BioResources*, 2016, **11**, 1270–1279, DOI: [10.15376/biores.11.1.1270-1279](https://doi.org/10.15376/biores.11.1.1270-1279).
- 31 N. N. Maseko, D. Enke, S. A. Iwarere, O. S. Oluwafemi and J. Pocock, Synthesis of low density and high purity silica xerogels from south african sugarcane leaves without the usage of a surfactant, *Sustainability*, 2023, **15**, 4626, DOI: [10.3390/su15054626](https://doi.org/10.3390/su15054626).
- 32 A. Espindola-Gonzalez, R. Fuentes-Ramirez, A. L. Martinez-Hernandez, V. M. Castano and C. Velasco-Santos, Structural characterization of silica particles extracted from grass stenotaphrum secundatum: Biotransformation via annelids, *Adv. Mater. Sci. Eng.*, 2014, **2014**, 956945, DOI: [10.1155/2014/956945](https://doi.org/10.1155/2014/956945).
- 33 C. V. Hoang, D. N. Thoai, N. T. D. Cam, T. T. T. Phuong, N. T. Lieu, T. T. T. Hien, D. N. Nhiem, T. D. Pham, M. H. T. Tung, N. T. T. Tran, A. Mechler and Q. V. Vo, Large-scale synthesis of nanosilica from silica sand for plant stimulant applications, *ACS Omega*, 2022, **7**, 41687–41695, DOI: [10.1021/acsomega.2c05760](https://doi.org/10.1021/acsomega.2c05760).
- 34 N. Meftah, A. Hani and A. Merdas, Extraction and physicochemical characterization of highly-pure amorphous silica nanoparticles from locally available dunes sand, *Chem. Afr.*, 2023, **6**, 3039–3048, DOI: [10.1007/s42250-023-00688-2](https://doi.org/10.1007/s42250-023-00688-2).
- 35 A. Lazaro, H. J. H. Brouwers, G. Quercia and J. W. Geus, The properties of amorphous nano-silica synthesized by the dissolution of olivine, *Chem. Eng. J.*, 2012, **211–212**, 112–121, DOI: [10.1016/j.cej.2012.09.042](https://doi.org/10.1016/j.cej.2012.09.042).
- 36 N. Raza, W. Raza, S. Madeddu, H. Agbe, R. V. Kumar and K. H. Kim, Synthesis and characterization of amorphous precipitated silica from alkaline dissolution of olivine, *RSC Adv.*, 2018, **8**, 32651–32658, DOI: [10.1039/C8RA06257A](https://doi.org/10.1039/C8RA06257A).
- 37 S. Stopic, C. Dertmann, I. Koiwa, D. Kremer, H. Wotruba, S. Etzold, R. Telle, P. Knops and B. Friedrich, Synthesis of nanosilica via olivine mineral carbonation under high pressure in an autoclave, *Metals*, 2019, **9**, 708, DOI: [10.3390/met9060708](https://doi.org/10.3390/met9060708).
- 38 C. N. M. Hoang, S. H. Nguyen and M. T. Tran, Nanoparticles in cancer therapy: Strategies to penetrate and modulate the tumor microenvironment – A review, *Smart Mater. Med.*, 2025, **6**, 270–284, DOI: [10.1016/j.smaim.2025.07.004](https://doi.org/10.1016/j.smaim.2025.07.004).



- 39 Q. Li, Z. Shi, M. Ou, Z. Li, M. Luo, M. Wu, X. Dong, L. Lu, F. Lv, F. Zhang and L. Mei, pH-labile artificial natural killer cells for overcoming tumor drug resistance, *J. Contr. Release*, 2022, **352**, 450–458, DOI: [10.1016/j.jconrel.2022.10.042](https://doi.org/10.1016/j.jconrel.2022.10.042).
- 40 Z. Li, Y. Yang, H. Wei, X. Shan, X. Wang, M. Ou, Q. Liu, N. Gao, H. Chen, L. Mei and X. Zeng, Charge-reversal biodegradable MSNs for tumor synergetic chemo/photothermal and visualized therapy, *J. Contr. Release*, 2021, **338**, 719–730, DOI: [10.1016/j.jconrel.2021.09.005](https://doi.org/10.1016/j.jconrel.2021.09.005).
- 41 S. Azat, A. V. Korobeinyk, K. Moustakas and V. J. Inglezakis, Sustainable production of pure silica from rice husk waste in Kazakhstan, *J. Clean. Prod.*, 2019, **217**, 352–359, DOI: [10.1016/j.jclepro.2019.01.142](https://doi.org/10.1016/j.jclepro.2019.01.142).
- 42 M. A. Abou Rida and F. Harb, Synthesis and characterization of amorphous silica nanoparticles from aqueous silicates using cationic surfactants, *J. Met., Mater. Miner.*, 2014, **24**, 37–42, DOI: [10.14456/jmmm.2014.7](https://doi.org/10.14456/jmmm.2014.7).
- 43 P. P. Nayak and A. K. Datta, Synthesis of SiO<sub>2</sub>-nanoparticles from rice husk ash and its comparison with commercial amorphous silica through material characterization, *Silicon*, 2021, **13**, 1209–1214, DOI: [10.1007/s12633-020-00509-y](https://doi.org/10.1007/s12633-020-00509-y).
- 44 A. Samuel, A. Abdullah, G. Xavier, S. Stephen, M. M. Zeidan, D. Choi and S. Abedrabbo, Sol-gel synthesis and characterization of ZnO-SiO<sub>2</sub> nanocomposites: a comparative study with pure ZnO and SiO<sub>2</sub>, *Nanoscale Adv.*, 2025, **7**, 7145–7155, DOI: [10.1039/D5NA00612K](https://doi.org/10.1039/D5NA00612K).
- 45 S. Supic, M. Malesev, V. Radonjanin, V. Bulatovic and T. Milovic, Reactivity and pozzolanic properties of biomass ashes generated by wheat and soybean straw combustion, *Materials (Basel)*, 2021, **14**, 1004, DOI: [10.3390/ma14041004](https://doi.org/10.3390/ma14041004).
- 46 A. Alhadhrami, G. G. Mohamed, A. H. Sadek, S. H. Ismail, A. A. Ebnalwaled and A. S. A. Almalki, Behavior of silica nanoparticles synthesized from rice husk ash by the sol-gel method as a photocatalytic and antibacterial agent, *Materials (Basel)*, 2022, **15**, 8211, DOI: [10.3390/ma15228211](https://doi.org/10.3390/ma15228211).
- 47 M. Naddaf, H. Kafa and I. Ghanem, Extraction and characterization of nano-silica from olive stones, *Silicon*, 2020, **12**, 185–192, DOI: [10.1007/s12633-019-00112-w](https://doi.org/10.1007/s12633-019-00112-w).
- 48 P. U. Nzereogu, A. D. Omah, F. I. Ezema, E. I. Iwuoha and A. C. Nwanya, Silica extraction from rice husk: Comprehensive review and applications, *Hybrid Adv.*, 2023, **4**, 100111, DOI: [10.1016/j.hybadv.2023.100111](https://doi.org/10.1016/j.hybadv.2023.100111).
- 49 T. Kaur, G. P. Singh, G. Kaur, S. Kaur and P. K. Gill, Synthesis of biogenic silicon/silica (Si/SiO<sub>2</sub>) nanocomposites from rice husks and wheat bran through various microorganisms, *Mater. Res. Express*, 2016, **3**, 085026, DOI: [10.1088/2053-1591/3/8/085026](https://doi.org/10.1088/2053-1591/3/8/085026).
- 50 M. A. Azmi, N. A. A. Ismail, M. Rizamarhaiza, W. M. Hasif and H. Taib, Characterisation of silica derived from rice husk (Muar, Johor, Malaysia) decomposition at different temperatures, *AIP Conf. Proc.*, 2016, **1756**, 020005, DOI: [10.1063/1.4958748](https://doi.org/10.1063/1.4958748).
- 51 R. P. Bagwe, L. R. Hilliard and W. Tan, Surface modification of silica nanoparticles to reduce aggregation and nonspecific binding, *Langmuir*, 2006, **22**, 4357–4362, DOI: [10.1021/la052797j](https://doi.org/10.1021/la052797j).
- 52 C. Y. Rahimzadeh, A. A. Barzinjy, A. S. Mohammed and S. M. Hamad, Green synthesis of SiO<sub>2</sub> nanoparticles from Rhus coriaria L. extract: Comparison with chemically synthesized SiO<sub>2</sub> nanoparticles, *PLoS One*, 2022, **17**, e0268184, DOI: [10.1371/journal.pone.0268184](https://doi.org/10.1371/journal.pone.0268184).
- 53 V. K. Yadav and M. H. Fulekar, Green synthesis and characterization of amorphous silica nanoparticles from fly ash, *Mater. Today: Proc.*, 2019, **18**, 4351–4359, DOI: [10.1016/j.matpr.2019.07.395](https://doi.org/10.1016/j.matpr.2019.07.395).
- 54 A. Mourhly, M. Khachani, A. El Hamidi, M. Kacimi, M. Halim and S. Arsalane, The synthesis and characterization of low-cost mesoporous silica SiO<sub>2</sub> from local pumice rock, *Nanomater. Nanotechnol.*, 2015, **5**, 35, DOI: [10.5772/62033](https://doi.org/10.5772/62033).
- 55 N. E. Villarreal, E. G. Martinez, E. P. Tijerina, F. V. Rodriguez and F. P. Delgado, Silica nanoparticles from agave distillate for the removal of the Methylene Blue dye from water, *J. Mater. Sci. Eng.*, 2025, **20**, 124, DOI: [10.1186/s40712-025-00322-8](https://doi.org/10.1186/s40712-025-00322-8).
- 56 O. I. Salako, J. J. Gonzalez, A. G. Cummins, J. L. Zambrano, B. Lewis, R. Lentz, Z. Lin, P. O. Aghadiuno, W. H. Stinson and D. V. Esposito, Zeta potential measurements of SiO<sub>2</sub> and TiO<sub>2</sub> particles in anionic and cationic surfactant solutions, *Surf. Interfaces*, 2026, **80**, 108180, DOI: [10.1016/j.surfin.2025.108180](https://doi.org/10.1016/j.surfin.2025.108180).
- 57 E. Akhayere and D. Kavaz, Nano-silica and nano-zeolite synthesized from barley grass straw for effective removal of gasoline from aqueous solution: a comparative study, *Chem. Eng. Commun.*, 2021, **208**, 1419–1435, DOI: [10.1080/00986445.2020.1786373](https://doi.org/10.1080/00986445.2020.1786373).
- 58 B. H. Hameed, A. T. M. Din and A. L. Ahmad, Adsorption of methylene blue onto bamboo-based activated carbon: Kinetics and equilibrium studies, *J. Hazard. Mater.*, 2007, **141**, 819–825, DOI: [10.1016/j.jhazmat.2006.07.049](https://doi.org/10.1016/j.jhazmat.2006.07.049).
- 59 R. Rajan, Y. Zakaria, S. Shamsuddin and N. F. N. Hassan, Robust synthesis of mono-dispersed spherical silica nanoparticle from rice husk for high definition latent fingerprint development, *Arab. J. Chem.*, 2020, **13**, 8119–8132, DOI: [10.1016/j.arabjc.2020.09.042](https://doi.org/10.1016/j.arabjc.2020.09.042).
- 60 M. C. D. Dominic, K. V. Neenu, P. M. S. Begum, R. Joseph, D. S. Rosa, Y. Duan, A. Balan, T. G. Ajithkumar, M. Soumya, A. Shelke, J. Parameswaranpillai and M. Badawi, Nanosilica from Averrhoa bilimbi juice pre-treated rice husk: Preparation and characterization, *J. Clean. Prod.*, 2023, **413**, 137476, DOI: [10.1016/j.jclepro.2023.137476](https://doi.org/10.1016/j.jclepro.2023.137476).

